Article

Measuring the knot of non-Hermitian degeneracies and non-commuting braids

https://doi.org/10.1038/s41586-022-04796-w

Received: 16 December 2021

Accepted: 25 April 2022

Published online: 13 July 2022

Check for updates

Yogesh S. S. Patil[1]✉, Judith Höller[1,2], Parker A. Henry[3], Chitres Guria[1], Yiming Zhang[1], Luyao Jiang[1], Nenad Kralj[1,4], Nicholas Read[1,3,5] & Jack G. E. Harris[1,3,5]✉

Any system of coupled oscillators may be characterized by its spectrum of resonance frequencies (or eigenfrequencies), which can be tuned by varying the system's parameters. The relationship between control parameters and the eigenfrequency spectrum is central to a range of applications[1–3]. However, fundamental aspects of this relationship remain poorly understood. For example, if the controls are varied along a path that returns to its starting point (that is, around a 'loop'), the system's spectrum must return to itself. In systems that are Hermitian (that is, lossless and reciprocal), this process is trivial and each resonance frequency returns to its original value. However, in non-Hermitian systems, where the eigenfrequencies are complex, the spectrum may return to itself in a topologically non-trivial manner, a phenomenon known as spectral flow. The spectral flow is determined by how the control loop encircles degeneracies, and this relationship is well understood for $N = 2$ (where N is the number of oscillators in the system)[4,5]. Here we extend this description to arbitrary N. We show that control loops generically produce braids of eigenfrequencies, and for $N > 2$ these braids form a non-Abelian group that reflects the non-trivial geometry of the space of degeneracies. We demonstrate these features experimentally for $N = 3$ using a cavity optomechanical system.

A very wide range of physical systems are described by first-order differential equations of motion that are linear in the system's coordinates. This includes classical systems near to mechanical equilibrium (for example, coupled oscillators and linear wave systems), closed quantum systems and open quantum systems that can be brought to Lindblad form. In these descriptions, the system's state is an N-dimensional complex vector whose time evolution is generated by an $N \times N$ complex matrix H (which we take to be traceless without loss of generality). The qualitative behaviour of such a system depends on the form of H, which reflects the relevant symmetries and conservation laws. For example, in the quantum description of closed systems, H is Hermitian. On the other hand, Newtonian mechanics and Maxwellian electromagnetism both allow for linear elements having non-reciprocity, gain and loss, and so the classical equations of motion for N coupled oscillators (whose positions and momenta are encoded as N complex numbers) may have H of any form.

Recent years have seen considerable interest in features that distinguish non-Hermitian systems from their Hermitian counterparts. These include non-orthogonal eigenvectors, complex eigenvalues and a type of degeneracy, known as an exceptional point (EP), at which H is non-diagonalizable. In addition, non-Hermitian systems respond to perturbations of H in a qualitatively different manner than Hermitian systems do[4,6,7]. These differences offer practical routes to new forms of control, sensing and robustness, and have been explored in optics, microwaves, electronics, acoustics, optomechanics and qubits[1–3,5,8–15].

Despite rapid progress, some fundamental aspects of non-Hermitian systems remain poorly understood. For example, when a system's parameters are varied around a closed loop (with this 'control loop' chosen so that the spectrum is non-degenerate throughout), the eigenvalues may move around one another in the complex plane. The way in which they do so, viewed topologically, is what we will describe below as 'spectral flow'. It is determined by the manner in which the control loop encloses degeneracies; however, the specific relationship between the loop, the degeneracies and the resulting spectral flow is well known only for $N = 2$. For $N > 2$, studies of spectral flow have focused on special cases in which H is constrained or on numerical simulations of specific systems, rather than on a general description of the spectral flow[16–24].

Control loops and spectral flow

For any N, the spectral flow can be described by regarding the spectrum of H as an unordered set $\boldsymbol{\lambda}$ of N points in the complex plane. We take the parameters controlling $\boldsymbol{\lambda}$ to be the $N-1$ complex coefficients in p_H, the characteristic polynomial of H. These coefficients define the 'control space' $\mathcal{L}_N \cong \mathbb{C}^{N-1}$. They smoothly parameterize the space of spectra, and have simple expressions in terms of the elements of H. $\mathcal{L}_N$ can be partitioned into two subspaces $\mathcal{V}_N$ and $\mathcal{G}_N$, corresponding respectively to whether or not the spectrum is degenerate. $\mathcal{V}_N$ consists of the points where D, the discriminant of p_H, vanishes (Methods).

[1]Department of Physics, Yale University, New Haven, CT, USA. [2]Howard Hughes Medical Institute, Janelia Research Campus, Ashburn, VA, USA. [3]Department of Applied Physics, Yale University, New Haven, CT, USA. [4]Niels Bohr Institute, University of Copenhagen, Copenhagen, Denmark. [5]Yale Quantum Institute, Yale University, New Haven, CT, USA. ✉e-mail: yogesh.patil@yale.edu; jack.harris@yale.edu

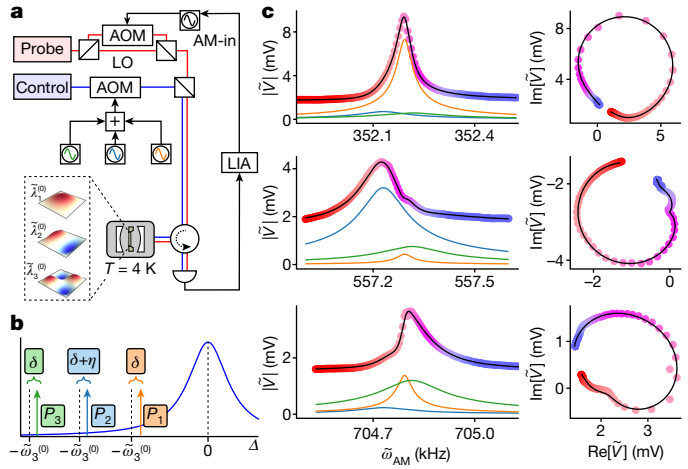

Fig. 1 | Experimental schematic and susceptibility measurement. **a**, Two lasers (red and blue paths) address two modes of an optical cavity (white) in a cryostat (grey). The cavity contains a Si_3N_4 membrane whose three mechanical modes are shown in the dashed box. AOM, acousto-optic modulator; LO, local oscillator; LIA, lock-in amplifier; AM-in, amplitude modulation input. **b**, The optical spectrum, showing the three control beams (green, light blue, orange) and the cavity mode (blue). The non-degeneracy of the bare modes in $\mathcal{R}$ is set by $\eta = -2\pi \times 100$ Hz. **c**, The complex response $\tilde{V}$ measured at frequencies $\bar{\omega}_{AM}$ near $\bar{\omega}_1^{(0)}$ (top), $\bar{\omega}_2^{(0)}$ (centre) and $\bar{\omega}_3^{(0)}$ (bottom). Here $\mathbf{\Psi} = (2\pi \times 50\ \text{kHz}, 125\,\mu\text{W}, 364\,\mu\text{W}, 426\,\mu\text{W})$. The left column shows $|\tilde{V}(\bar{\omega}_{AM})|$ and the right column shows a parametric plot of $\tilde{V}(\bar{\omega}_{AM})$. The data points are coloured by $\bar{\omega}_{AM}$ (the $1-\sigma$ confidence intervals are smaller than the plotted points). A global fit (black lines) gives the system's eigenvalues. The magnitude of each mode's contribution (determined from the fit) is shown as the orange, light blue and green curves in the left column.

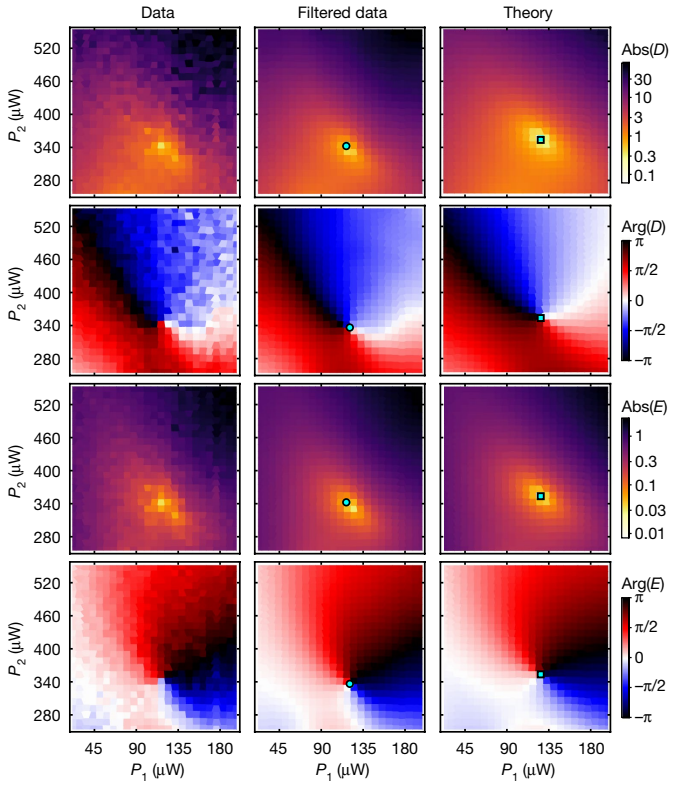

Fig. 2 | Locating EP_2 points on the hypersurface $\mathcal{S}$. The complex-valued quantities D and E measured on a typical 2D sheet in the hypersurface $\mathcal{S}$. Abs and Arg denote the magnitude and argument of a complex number. The units of D are $10^{10} \times (2\pi\ \text{Hz})^6$. For this sheet, $P_3 = 78\ \mu\text{W}$ and $\delta = 2\pi \times 60$ kHz. Left column, raw data. Middle column, data after outlier rejection and smoothing (Supplementary Information). Cyan circles show algorithmically identified $\mathbf{\Psi}_{EP2}$. Right column, D and E calculated from optomechanics theory. Cyan squares, $\mathbf{\Psi}_{EP2}$ determined from this calculation. Data from the other 60 sheets are shown in the Supplementary Information.

Although $\mathcal{L}_N$ is topologically trivial, this need not be the case for $\mathcal{G}_N$ and $\mathcal{V}_N$. To describe these two subspaces, we note that varying the control parameters along a smooth curve $C \subset \mathcal{G}_N$ causes the N points in $\boldsymbol{\lambda}$ to be smoothly transported in the complex plane[4]. Throughout, we take C to be a closed curve (or 'loop'); we also fix a basepoint in $\mathcal{G}_N$ and consider only loops starting and ending at that point. In this case, traversing a loop C causes the initial spectrum to be smoothly transported back to itself. Such an evolution of N distinct points in the complex plane is called a braid of N strands (for example, ref. [25]). We will say that two braids are isotopic to one another if one of them can be continuously deformed into the other, keeping its endpoints fixed and its strands non-intersecting during the deformation. We define the spectral flow produced by a control loop C to be the isotopy equivalence class b of the corresponding braid of eigenvalues. Braids with the common basepoint can be concatenated to produce another such braid, and with that operation the bs form a group B_N, the Artin braid group[26].

Two isotopic braids arise from two control loops C_1, C_2 that can be continuously deformed into each other within $\mathcal{G}_N$, and hence each b corresponds to a homotopy class[27] ℓ of based loops $C \subset \mathcal{G}_N$. Concatenating Cs gives a group operation on the ℓs, which thus form the fundamental group[27] π_1 of the space $\mathcal{G}_N$. It follows from this discussion that $\pi_1(\mathcal{G}_N) \cong B_N$ (refs. [28–30]). Because $\mathcal{L}_N$ is topologically trivial, the non-trivial $\pi_1(\mathcal{G}_N)$ arises solely because $\mathcal{V}_N$ (consisting of the points at which the spectrum is degenerate) was removed from $\mathcal{L}_N$ to produce $\mathcal{G}_N$, leaving a hole that control loops can wind around in various (non-homotopic) ways that correspond to the elements of π_1.

To give a concrete picture of $\mathcal{G}_N$ and $\mathcal{V}_N$ (and the ways in which loops in the former may encircle the latter), we note that for $N = 2$, the reasoning above returns the familiar result $\mathcal{G}_2 \cong \mathbb{C} \setminus \{0\}$ (the complex plane without the origin). The fundamental group of this space, $\pi_1(\mathcal{G}_2)$, is isomorphic to $B_2 \cong \mathbb{Z}$ (the group of integers under addition), reflecting the fact that each loop in $\mathcal{G}_2$ belongs to the ℓ determined by its winding number and concatenating loops results in a new loop whose winding number is the sum of the winding numbers of the concatenated loops.

For $N = 3$, we have $\mathcal{G}_3 \cong \mathbb{C}^2 - \mathcal{V}_3$ and $\pi_1(\mathbb{C}^2 - \mathcal{V}_3) \cong B_3$. From the equation $D = 0$ we show in the Methods that $\mathcal{V}_3$ is a connected hypersurface that includes a singular point at the origin (0,0) corresponding to threefold degeneracy; the rest of $\mathcal{V}_3$ consists of the twofold degeneracies. The twofold degeneracies form the space $\mathcal{K} \times \mathbb{R}_{>0}$, where $\mathcal{K}$ is the trefoil knot and $\mathbb{R}_{>0}$ plays the role of the radial distance from the threefold degeneracy. Therefore, if we identify $\mathbb{C}^2$ with $\mathbb{R}^4$, intersecting $\mathcal{V}_3$ with a real hypersphere $\mathcal{S}^3$ centred at the origin gives $\mathcal{K}$. This structure (which is shown in Extended Data Fig. 1) agrees with the fact that $\pi_1(\mathcal{S}^3 - \mathcal{K}) \cong B_3$.

This description highlights two important features common to all non-Hermitian systems with $N > 2$, but absent in the well-studied case $N = 2$. The first is that the subspace $\mathcal{V}_N$ has a non-trivial geometry. The second is that this geometry makes loops in $\mathcal{G}_N$ non-commutative (as B_N is non-Abelian for $N > 2$). This rich behaviour reflects the fact that $\boldsymbol{\lambda}$ consists of the roots of p_H, and non-Hermitian systems can realize any complex polynomial as p_H. In the mathematical context of complex polynomial equations, the braid and knot structures described here are well-known features of the relation between a polynomial's coefficients and its roots.

Here, we provide an experimental demonstration of these two features. We use a three-mode mechanical system in which H is tuned by control parameters $\mathbf{\Psi}$ that span $\mathcal{L}_3$ and so provide access to a threefold degeneracy and all the spectra in its neighbourhood[6]. We measure spectra on a hypersurface surrounding the threefold degeneracy,

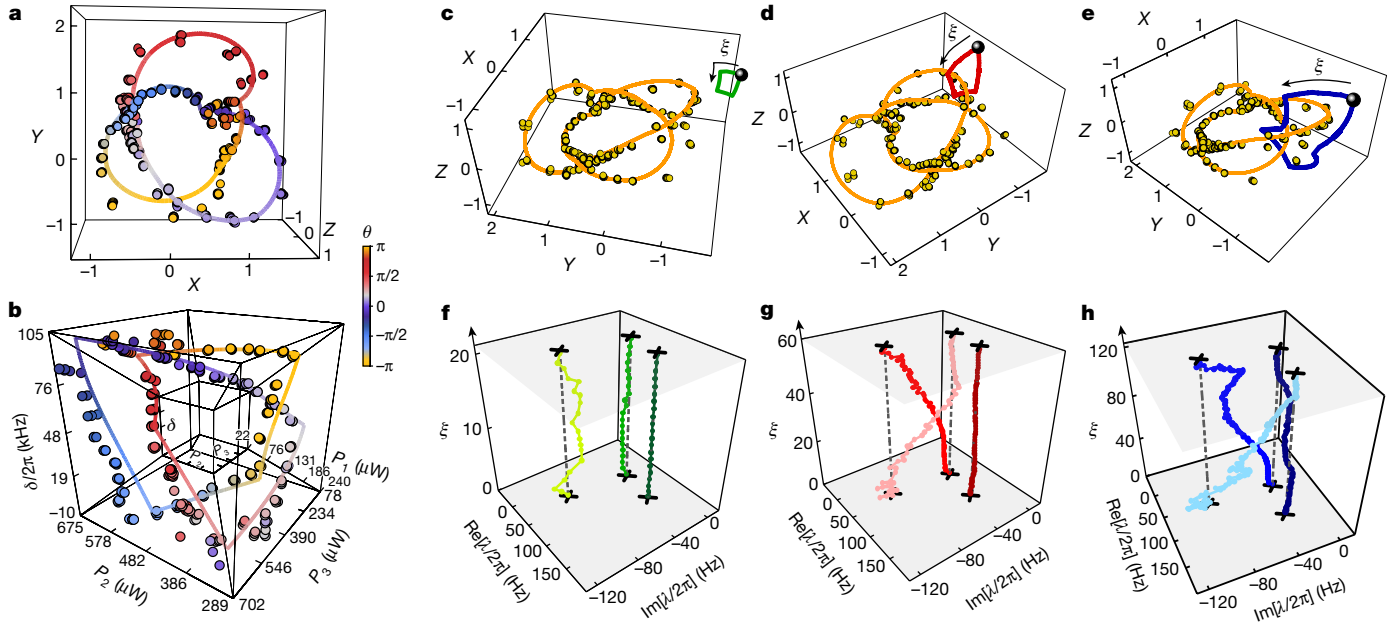

Fig. 3 | Measurements of the EP_2 knot $\mathcal{K}$ and the eigenvalue braids. a, All of the EP_2 locations ($\mathbf{\Psi}_{EP2}$) shown in a stereographic projection of $\mathcal{S}$. X, Y and Z are dimensionless combinations of the control parameters. **b**, The data from **a** in a projection where each of the six 'faces' of $\mathcal{S}$ that contains $\mathbf{\Psi}_{EP2}$ is linearly mapped to one of the hexahedrons surrounding the central cube. The solid curve in **a** and **b** is the best fit to the data. Details of the projections and fit are in the Methods. The coordinate θ is described in the Supplementary Information. Additional views of these data are in Extended Data Fig. 5. **c**–**e**, Three control loops (green (**c**), red (**d**), blue (**e**)) in $\mathcal{S}$, each from a different ℓ and sharing a common basepoint (black sphere). The measured knot $\mathcal{K}$ (yellow circles) and the best-fit knot (orange curve) are shown for reference. The projection is the same as in **a**. **f**–**h**, The eigenvalue spectrum $\boldsymbol{\lambda}(\mathbf{\Psi})$ as $\mathbf{\Psi}$ is varied around the corresponding loop from **c**–**e**. ξ indexes the values of $\mathbf{\Psi}$ along each loop. The black crosses show $\boldsymbol{\lambda}$ at the basepoint. The dashed lines are guides to the eye. The $1-\sigma$ confidence intervals for $\boldsymbol{\lambda}$ are comparable to the size of the plotted points. The measured $\boldsymbol{\lambda}$ traces out the braids: $\mathbb{I}$ (**f**), σ_1 (**g**) and $\sigma_2\sigma_1$ (**h**). Extended Data Fig. 10 shows the control loops, and Extended Data Fig. 6 shows a comparison with theory. Animations of this figure are shown in Supplementary Videos 3 and 4.

and find the trefoil knot $\mathcal{K}$ formed by the twofold degeneracies. We show that varying $\mathbf{\Psi}$ around a loop produces an eigenvalue braid whose spectral flow is determined by how the loop encircles $\mathcal{K}$. We demonstrate braids that can be concatenated to produce any element of B_3, and show the non-commutation of these braids. These features are demonstrated using a cavity optomechanical system, although we emphasize that they are generic to oscillators realized in any physical domain.

Experimental system

The experiment is shown schematically in Fig. 1a. It uses three vibrational modes of a Si_3N_4 membrane. The dynamical matrix H governing these modes is controlled by placing the membrane in an optical cavity and using the dynamical back-action (DBA) effect of cavity optomechanics[31]. In the absence of DBA, the three modes have resonance frequencies $(\widetilde{\omega}_1^{(0)}, \widetilde{\omega}_2^{(0)}, \widetilde{\omega}_3^{(0)}) = 2\pi \times (352, 557, 705)$ kHz and optomechanical coupling rates $\boldsymbol{g} = (g_1, g_2, g_3) = 2\pi \times (0.198, 0.304, 0.300)$ Hz. The cavity linewidth $\kappa = 2\pi \times 190$ kHz. Three tones produced from a single laser ('control' in Fig. 1a) drive the cavity with powers $P_{1,2,3}$. The tones' relative detunings are fixed (Fig. 1b), and their beatnotes define a rotating frame $\mathcal{R}$ in which the three modes' eigenvalues are almost degenerate for $P_i = 0$. Within $\mathcal{R}$, the control parameters $\mathbf{\Psi} = (\delta, P_1, P_2, P_3)$ (where δ is the tones' common detuning, Fig. 1b) can tune the system to a threefold degeneracy. They also provide linearly independent control of the coefficients of p_H (Methods and Supplementary Information), and hence span $\mathcal{L}_3$. H is otherwise unconstrained, so it accesses degeneracies of the most generic type (for a given order): that is, at an m-order degeneracy, the Jordan normal form of H contains a Jordan block of dimension m (we call such a point EP_m).

The modes' eigenvalue spectrum $\boldsymbol{\lambda}$ is determined by measuring the membrane's mechanical susceptibility. This is accomplished using a second laser ('probe' in Fig. 1a) to exert an oscillatory force on the membrane (at frequency $\widetilde{\omega}_{AM}$), and to record a heterodyne signal $\widetilde{V}$ proportional to the membrane's response. Figure 1c shows a typical measurement of $\widetilde{V}(\widetilde{\omega}_{AM})$, along with a fit of these data to standard optomechanics theory. This fit returns the complex eigenvalues λ_i, as well as the amplitudes $s_{i,j}$ (denoting the contribution of the jth mode to the peak near $\widetilde{\omega}_i^{(0)}$). In the remainder of this paper, $\boldsymbol{\lambda}$ is determined from data and fits as in Fig. 1c.

Locating degeneracies

The system's EP_3 is identified by measuring $\boldsymbol{\lambda}(\mathbf{\Psi})$ and converting each $\boldsymbol{\lambda}$ to $d = |\lambda_1 - \lambda_2| + |\lambda_2 - \lambda_3| + |\lambda_3 - \lambda_1|$ (Methods). As shown in Extended Data Figs. 2 and 3, measurements of $d(\mathbf{\Psi})$ give $\mathbf{\Psi}_{EP3} = (2\pi \times 54(7)$ kHz, 128(8) μW, 428(3) μW, 304(15) μW), in good agreement with the value calculated from the independently measured device parameters (Methods).

To study the spectrum on a hypersurface surrounding $\mathbf{\Psi}_{EP3}$, we measured $\boldsymbol{\lambda}$ on the boundary of a four-dimensional (4D) hyperrectangle $\mathcal{S}$ centred close to $\mathbf{\Psi}_{EP3}$. Specifically, $\mathcal{S}$ bounds the region: -10 kHz $\le \delta/2\pi \le 106$ kHz, 22 μW $\le P_1 \le 240$ μW, 289 μW $\le P_2 \le 675$ μW, 78 μW $\le P_3 \le 702$ μW. It consists of eight three-dimensional (3D) 'faces', each corresponding to fixing the value of one control parameter. $\mathbf{\Psi}$ was densely rastered over 61 distinct two-dimensional (2D) 'sheets' within $\mathcal{S}$ (Extended Data Fig. 4). Data from a typical sheet are shown in Fig. 2. For each value of $\mathbf{\Psi}$ (that is, for each pixel in the sheet), $\widetilde{V}(\widetilde{\omega}_{AM})$ was measured and fit as in Fig. 1c.

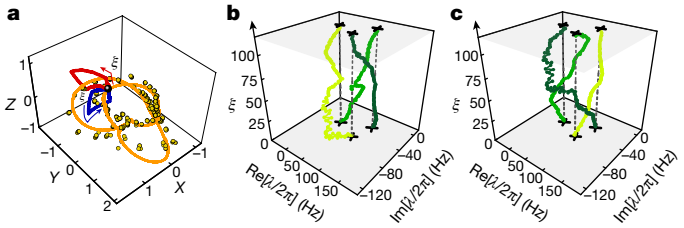

Fig. 4 | Non-commutation of control loops. a, Two loops (red, blue) belonging to different ℓ. They are non-intersecting, except that they have a common basepoint (black sphere). The measured knot $\mathcal{K}$ (yellow circles) and the best-fit knot (orange curve) are shown for reference. The projection is the same as in Fig. 3a. **b**, The spectrum $\boldsymbol{\lambda}(\boldsymbol{\Psi})$ as $\boldsymbol{\Psi}$ is varied around the loop formed by concatenating the two loops in **a**. Specifically, the red loop is traversed first ($1 \le \xi \le 59$), and then the blue loop ($60 \le \xi \le 116$). The black crosses show $\boldsymbol{\lambda}$ at the basepoint. The dashed lines are guides to the eye, and the $1-\sigma$ confidence intervals for $\boldsymbol{\lambda}$ are comparable to the size of the plotted points. **c**, The spectrum $\lambda(\boldsymbol{\Psi})$ as $\boldsymbol{\Psi}$ is varied first around the blue loop ($1 \le \xi \le 57$), and then the red loop ($58 \le \xi \le 116$). In both cases, the loops are traversed in the sense indicated by the arrows in **a**.

To locate the EP_2 points in $\mathcal{S}$ we considered two quantities derived from these fits: $D = (\lambda_1 - \lambda_2)^2(\lambda_2 - \lambda_3)^2(\lambda_3 - \lambda_1)^2$ and $E = (\det[S])^{-2}$ where S is the matrix formed by the $s_{i,j}$. Both D and E vanish at EP_2, and both exhibit a phase winding of 2π around EP_2. However, they provide complementary information: $D = 0$ reflects eigenvalue degeneracy, whereas $E = 0$ reflects eigenvector degeneracy (Supplementary Information). Furthermore, D and E are derived from different aspects of the fits to $\widetilde{V}(\widetilde{\omega}_{AM})$, and so reflect partially independent features of the data. The locations ($\boldsymbol{\Psi}_{EP2}$) of the zeroes and phase windings in D and E are identified algorithmically (Supplementary Information) and are shown in Fig. 2 as cyan circles.

The knot of twofold degeneracies

Figure 3a,b show all of the $\boldsymbol{\Psi}_{EP2}$ identified in this way. For ease of visualization, they are depicted using two projections of $\mathcal{S}$, both of which generically preserve knot equivalence classes. Figure 3a uses a stereographic projection, whereas Fig. 3b uses a projection isomorphic to the one in Fig. 3a, but which is more easily connected to the control parameters. In both projections, the experimentally identified EP_2s are seen to trace out a curve that forms a trefoil knot $\mathcal{K}$. Each point in Fig. 3a,b is coloured according to the value of θ measured at the corresponding $\boldsymbol{\Psi}_{EP2}$ (θ is derived from $\boldsymbol{\lambda}$ as defined in the Supplementary Information, and serves as a coordinate along $\mathcal{K}$).

Figure 3a,b also show the best fit of the measured $\boldsymbol{\Psi}_{EP2}$ to standard optomechanics theory (Methods). This fit uses $\boldsymbol{g}$ and κ as parameters and returns $\boldsymbol{g} = 2\pi \times (0.1979, 0.3442, 0.3092)$ Hz and $\kappa = 2\pi \times 173.84$ kHz (these values are also used to generate the plots of D and E (labelled 'theory') in the right-hand column of Fig. 2). These values of $\boldsymbol{g}$ and κ extracted by fitting the knot $\mathcal{K}$ in the three-mode spectrum agree well with the values given earlier (in the section 'Experimental system'), which are determined independently from measurements of the DBA (Extended Data Fig. 9 and Supplementary Information).

Non-commuting eigenvalue braids

When $\boldsymbol{\Psi}$ is varied around a loop C from a given ℓ, $\boldsymbol{\lambda}(\boldsymbol{\Psi})$ is expected to form a braid whose equivalence class b is determined by ℓ. To demonstrate this, we selected pixels from the dataset described above (the 61 sheets) that trace out three loops with a common basepoint, as shown in Fig. 3c–e. The corresponding $\boldsymbol{\lambda}(\boldsymbol{\Psi})$ for each loop is shown in Fig. 3f–h. The loops belong to different ℓ, and result in eigenvalue braids from $b = \mathbb{I}, \sigma_1, \sigma_2\sigma_1$ (Fig. 3f–h, respectively). Here, $\mathbb{I}$ is the identity, σ_i (σ_i^{-1}) indicates that strand i has crossed over (under) strand $i+1$, the strands are counted from the left (in the view used for the figures), and operations are written symbolically from right to left as the braid is read from bottom to top[25]. As σ_1 and $\sigma_2\sigma_1$ together generate the group B_3, the loops in Fig. 3d,e can be concatenated to produce any braid of eigenvalues. The correspondence between a loop's ℓ and the b it produces is a robust feature of the data; this is illustrated in Fig. 4 and Extended Data Fig. 7, which show the braids produced by several other loops.

The non-Abelian character of the group formed by these braids is demonstrated in Fig. 4. Figure 4a shows two loops (red, blue) belonging to different ℓ. Figure 4b shows $\boldsymbol{\lambda}(\boldsymbol{\Psi})$ as $\boldsymbol{\Psi}$ is stepped first around the red loop and then around the blue loop, whereas Fig. 4c shows $\boldsymbol{\lambda}(\boldsymbol{\Psi})$ as $\boldsymbol{\Psi}$ is stepped first around the blue loop and then around the red loop. The former gives $b = \sigma_2^{-1}\sigma_1^{-1}$, whereas the latter gives $b = \sigma_1^{-1}\sigma_2^{-1}$. The inequivalence of these braids, which can be seen directly from the fact that they result in different permutations of the eigenvalues, demonstrates that encircling a degeneracy is not characterized by a number (as is the case for $N = 2$), but by a braid equivalence class.

Future directions

Looking ahead, one may ask if the braids demonstrated here may play a role in the system's dynamics. For example, if one eigenmode of the system is initially excited, and then the system is slowly evolved around a control loop, it might be expected that the excitation would remain in the eigenmode that is smoothly connected with the original one, in analogy with adiabatic transport in Hermitian systems. If this were the case, a control loop would permute excitations among the normal modes, with the specific permutation determined by the loop's ℓ. Such a control scheme—in which the outcome is determined by a topological property of the input—would be of considerable interest. However, in non-Hermitian systems adiabatic control loops do not transport excitations in this manner[32]. On the other hand, real-time loops have been shown to produce similar transport in special cases[13,14,33,34], and it remains an open question whether control schemes such as 'shortcuts to adiabaticity'[35–37] or tailored nonlinearities[12,38–40] can stabilize such transport more generally. Exploration of these possibilities may open new means for achieving robust topological control in oscillator systems.

Online content

Any methods, additional references, Nature Research reporting summaries, source data, extended data, supplementary information, acknowledgements, peer review information; details of author contributions and competing interests; and statements of data and code availability are available at https://doi.org/10.1038/s41586-022-04796-w.

1. El-Ganainy, R. et al. Non-Hermitian physics and PT symmetry. *Nat. Physics* **14**, 11–19 (2018).
2. Miri, M.-A. & Alù, A. Exceptional points in optics and photonics. *Science* **363**, eaar7709 (2019).
3. Wiersig, J. Review of exceptional point-based sensors. *Photon. Res.* **8**, 1457–1467 (2020).
4. Kato, T. *Perturbation Theory for Linear Operators* (Springer-Verlag, 1995).
5. Dembowski, C. et al. Experimental observation of the topological structure of exceptional points. *Phys. Rev. Lett.* **86**, 787–790 (2001).
6. Arnold, V. I. On matrices depending on parameters. *Russ. Math. Surv.* **26**, 29–43 (1971).
7. Gilmore, R. *Catastrophe Theory for Scientists and Engineers* 345–366 (John Wiley & Sons, Inc., 1981).
8. Ota, Y. et al. Active topological photonics. *Nanophotonics* **9**, 547–567 (2020).
9. Bahari, B. et al. Nonreciprocal lasing in topological cavities of arbitrary geometries. *Science* **358**, 636–640 (2017).
10. Naghiloo, M., Abbasi, M., Joglekar, Y. N. & Murch, K. M. Quantum state tomography across the exceptional point in a single dissipative qubit. *Nat. Physics* **15**, 1232–1236 (2019).
11. Zhong, Q., Özdemir, S. K., Eisfeld, A., Metelmann, A. & El-Ganainy, R. Exceptional-point-based optical amplifiers. *Phys. Rev. Appl.* **13**, 014070 (2020).
12. Assawaworrarit, S., Yu, X. & Fan, S. Robust wireless power transfer using a nonlinear parity–time-symmetric circuit. *Nature* **546**, 387–390 (2017).

13. Xu, H., Mason, D., Jiang, L. & Harris, J. G. E. Topological energy transfer in an optomechanical system with an exceptional point. *Nature* **537**, 80–83 (2016).
14. Doppler, J. et al. Dynamically encircling an exceptional point for asymmetric mode switching. *Nature* **537**, 76–79 (2016).
15. Gao, T. et al. Observation of non-Hermitian degeneracies in a chaotic exciton-polariton billiard. *Nature* **526**, 554–558 (2015).
16. Graefe, E.-M., Günther, U., Korsch, H. J. & Niederle, A. E. A non-Hermitian PT-symmetric Bose–Hubbard model: eigenvalue rings from unfolding higher-order exceptional points. *J. Phys. A: Math. Theoret.* **41**, 255206 (2008).
17. Heiss, W. D. Chirality of wavefunctions for three coalescing levels. *J.Phys. A: Math. Theoret.* **41**, 244010 (2008).
18. Cartarius, H., Main, J. & Wunner, G. Exceptional points in the spectra of atoms in external fields. *Phys. Rev. A* **79**, 053408 (2009).
19. Demange, G. & Graefe, E.-M. Signatures of three coalescing eigenfunctions. *J. Phys. A: Math. Theor* **45**, 025303 (2011).
20. Lee, S.-Y., Ryu, J.-W., Kim, S. W. & Chung, Y. Geometric phase around multiple exceptional points. *Phys. Rev. A* **85**, 064103 (2012).
21. Ryu, J.-W., Lee, S.-Y. & Kim, S. W. Analysis of multiple exceptional points related to three interacting eigenmodes in a non-Hermitian Hamiltonian. *Phys. Rev. A* **85**, 042101 (2012).
22. Zhen, B. et al. Spawning rings of exceptional points out of Dirac cones. *Nature* **525**, 354 (2015).
23. Ding, K., Zhang, Z. Q. & Chan, C. T. Coalescence of exceptional points and phase diagrams for one-dimensional PT-symmetric photonic crystals. *Phys. Rev. B* **92**, 235310 (2015).
24. Ding, K., Ma, G., Xiao, M., Zhang, Z. Q. & Chan, C. T. Emergence, coalescence, and topological properties of multiple exceptional points and their experimental realization. *Phys. Rev. X* **6**, 021007 (2016).
25. Wu, Y.-S. General theory for quantum statistics in two dimensions. *Phys. Rev. Lett.* **52**, 2103–2106 (1984).
26. Artin, E. Theory of braids. *Ann. Math.* **48**, 101–126 (1947).
27. Hatcher, A. *Algebraic Topology* (Cambridge Univ. Press, 2002).
28. Hurwitz, A. Ueber Riemann'sche Flächen mit gegebenen Verzweigungspunkten. *Math. Ann.* **39**, 1–60 (1891).
29. Fox, R. & Neuwirth, L. The braid groups. *Math. Scand.* **10**, 119–126 (1962).
30. Arnold, V. I. in *Vladimir I. Arnold, Collected Works* Vol. II (eds Givental, A. B. et al.) 199–220 (Springer-Verlag, 2014).
31. Aspelmeyer, M., Kippenberg, T. J. & Marquardt, F. Cavity optomechanics. *Rev. Mod. Phys.* **86**, 1391–1452 (2014).
32. Nenciu, G. & Rasche, G. On the adiabatic theorem for nonself-adjoint Hamiltonians. *J. Phys. A* **25**, 5741 (1992).
33. Uzdin, R., Mailybaev, A. & Moiseyev, N. On the observability and asymmetry of adiabatic state flips generated by exceptional points. *J. Phys. A* **44**, 435302 (2011).
34. Berry, M. V. & Uzdin, R. Slow non-Hermitian cycling: exact solutions and the Stokes phenomenon. *J. Phys. A* **44**, 435303 (2011).
35. Emmanouilidou, A., Zhao, X. G., Ao, P. & Niu, Q. Steering an Eigenstate to a destination. *Phys. Rev. Lett.* **85**, 1626 (2000).
36. Berry, M. V. Transitionless quantum driving. *J. Phys. A* **42**, 365303 (2009).
37. Ibáñez, S., Martínez-Garaot, S., Chen, X., Torrontegui, E. & Muga, J. G. Shortcuts to adiabaticity for non-Hermitian systems. *Phys. Rev. A* **84**, 023415 (2011).
38. Wu, B., Liu, J. & Niu, Q. Geometric phase for adiabatic evolutions of general quantum states. *Phys. Rev. Lett.* **94**, 140402 (2005).
39. Graefe, E.-M. & Korsch, H. J. Crossing scenario for a nonlinear non-Hermitian two-level system. *Czech. J. Phys.* **56**, 1007–1020 (2006).
40. Wang, H., Assawaworrarit, S. & Fan, S. Dynamics for encircling an exceptional point in a nonlinear non-Hermitian system. *Optic. Lett.* **44**, 638–641 (2019).

Methods

Characteristic polynomial, discriminant and the trefoil knot

For an $N \times N$ matrix H, the eigenvalues are the solutions of the characteristic equation $\det(\lambda I - H) = 0$, which can be written as

$$\lambda^N - a_1\lambda^{N-1} + a_2\lambda^{N-2} + \cdots + (-1)^N a_N = 0.$$

The coefficients a_i are invariants of H under similarity transforms (change of basis), and in particular $a_1 = \mathrm{tr}\, H$ and $a_N = \det H$. The characteristic polynomial on the left-hand side of this equation can be factored as $\prod_{i=1}^{N}(\lambda - \lambda_i)$ in which the roots λ_i may be repeated. The coefficients a_i are the elementary symmetric polynomials in the roots λ_i, namely $a_1 = \sum_{i=1}^{N}\lambda_i$, $a_2 = \sum_{i,j:i<j}\lambda_i\lambda_j$, ..., $a_N = \prod_{i=1}^{N}\lambda_i$.

The discriminant of the polynomial is defined as $D = \prod_{i<j}(\lambda_i - \lambda_j)^2$; it vanishes if any two roots of the polynomial are equal. Being a symmetric polynomial, it can be expressed algebraically in terms of the elementary symmetric polynomials a_i (for example, ref. [41]). The explicit expressions are simpler if we shift H by a multiple of the identity so that $a_1 = \mathrm{tr}H = 0$. Then for the quadratic, $N = 2$, the discriminant is the familiar expression $D = -4a_2$, and the roots are $\pm\sqrt{-a_2}$. Focusing hereafter on the cubic, $N = 3$, its discriminant is[41]

$$D = -4a_2^3 - 27a_3^2,$$

which enters the formulas for the roots.

Defining $x = a_3$, $y = -a_2$ as our coordinates in $\mathbb{C}^2$ (so that the characteristic polynomial is $p_H = \lambda^3 - y\lambda - x$), the solutions to the equation $D(x, y) = 4y^3 - 27x^2 = 0$ form an algebraic variety (a hypersurface) in $\mathbb{C}^2$ that has a singularity at $x = y = 0$. D has a (weighted) scaling property, such that rescaling $x \to ax$, $y \to by$, where a, b are real and positive and $a^2 = b^3$, changes D by a factor; this maps any non-zero solution to $D = 0$ to another. Thus the variety resembles a cone in $\mathbb{C}^2 \cong \mathbb{R}^4$, and it is sufficient to consider a cross section, that is the intersection of the variety with a hypersurface that (1) has the topology of a hypersphere $\mathcal{S}^3$, (2) surrounds the origin without passing through it or intersecting itself and (3) is everywhere transverse to the local action of an infinitesimal (say, by $a = 1 + \varepsilon, \varepsilon$ small) scaling. Any two such hypersurfaces are isotopy equivalent (through a rescaling that depends on position on the hypersurface). A particular such hypersurface[42] results from considering the unit hypersphere defined by $|x|^2 + |y|^2 = 1$. The points (x, y) on the hypersphere that satisfy $D(x, y) = 0$ can be parameterized as $(x, y) = (r_x e^{3i\theta}, r_y e^{2i\theta})$, where r_x, r_y are real positive constants and $0 \le \theta < 2\pi$ is a variable. These points lie on a two-torus T^2 embedded in $\mathcal{S}^3$, and form a closed curve that is a trefoil knot in this $\mathcal{S}^3$ (ref. [42]). This is illustrated in Extended Data Fig. 1, as described in the Supplementary Information.

For any knot or link in $\mathbb{R}^3$ or $\mathcal{S}^3$, the fundamental group of its complement is an isotopy invariant of the knot or link called the knot group. The knot group of the trefoil is well known to be the braid group B_3, or this can be inferred by reasoning as in the main text.

Experimental setup

As described in the main text, this experiment focuses on three vibrational modes of a Si_3N_4 membrane. The membrane's dimensions are 1 mm × 1 mm × 50 nm. These modes' bare eigenvalues (that is, in the absence of optomechanical effects) are $\tilde{\boldsymbol{\lambda}}^{(0)} = (\tilde{\lambda}_1^{(0)}, \tilde{\lambda}_2^{(0)}, \tilde{\lambda}_3^{(0)}) = 2\pi \times (352243 - 2.2\mathrm{i},\ 557217 - 1.9\mathrm{i},\ 704837 - 1.8\mathrm{i})$ Hz, where the real (imaginary) parts give each mode's oscillation frequency (amplitude damping rate). Frequencies related to the mechanical modes are denoted with a tilde when given in the laboratory frame, and without a tilde in the frame $\mathcal{R}$ described below.

The dynamical matrix $\widetilde{H}$ governing these modes is controlled using the DBA effect of cavity optomechanics[31]. The membrane is placed in an optical cavity with linewidth $\kappa/2\pi = 190$ kHz, input coupling rate $\kappa_{\mathrm{in}} = 0.267\kappa$ and optomechanical coupling rates $\boldsymbol{g} = (g_1, g_2, g_3) = 2\pi \times (0.198, 0.304, 0.300)$ Hz. Further details of the apparatus are in the Supplementary Information, Extended Data Fig. 8 and ref. [43].

The cavity is driven with three tones produced from a single laser ('control', Fig. 1a). The DBA from each tone induces a complex-valued shift in each mechanical mode's eigenvalue[31]. In addition, each pair of tones gives rise to an intracavity beatnote, which induces a complex-valued coupling between pairs of modes whose frequency difference is comparable to the beatnote frequency[44,45]. In the resolved sideband regime ($\kappa \ll \tilde{\omega}_{1,2,3}^{(0)}$, where $\tilde{\omega}_i^{(0)} \equiv \mathrm{Re}(\tilde{\lambda}_i^{(0)})$) these shifts and couplings can be tuned over the complex plane by varying the tones' powers P_k and detunings Δ_k ($k \in \{1, 2, 3\}$). An expression for $\widetilde{H}$ in terms of $P_k, \Delta_k, \kappa, \kappa_{\mathrm{in}}, \boldsymbol{g}$ and $\tilde{\boldsymbol{\lambda}}^{(0)}$ is given in the Supplementary Information. For the experiments described here, the tones' common detuning δ (Fig. 1b) is varied. Their relative detunings are fixed, and are chosen to produce beatnote frequencies close to the differences between the $\tilde{\omega}_i^{(0)}$.

The beatnote frequencies are chosen so that there is a rotating frame $\mathcal{R}$ (defined in the Supplementary Information) in which the dynamical matrix H is time-independent (in the rotating wave approximation), and in which the bare eigenvalues $\boldsymbol{\lambda}^{(0)}$ are almost degenerate (their non-degeneracy in $\mathcal{R}$ is set by $\eta = -2\pi \times 100$ Hz (Fig. 1b)).

Thus, within $\mathcal{R}$, the mechanical modes can be described by the equation of motion

$$\dot{\mathbf{x}}(t) = -\mathrm{i}H(\boldsymbol{\Psi})\mathbf{x}(t) + \mathbf{f}(t)$$

Here $\mathbf{x}(t) = (x_1(t), x_2(t), x_3(t))^{\mathrm{T}}$ and $\mathbf{f}(t) = (f_1(t), f_2(t), f_3(t))^{\mathrm{T}}$ are the modes' complex-valued amplitudes and the external forces driving them. Whereas the above equation is the generic equation of motion for any linear system, we emphasize the form of $H(\boldsymbol{\Psi})$ realized here: specifically, that the controls $\boldsymbol{\Psi}$ completely and smoothly parametrize all of the complex eigenspectra in a neighbourhood that includes EP_3 (ref. [6]).

Locating the EP_3

This section gives the protocol for experimentally identifying the EP_3. Approaches to identifying threefold degeneracies are also given in refs. [16–24,46–48].

We identify the value of control parameters ($\boldsymbol{\Psi}_{EP3}$) that corresponds to EP_3 through the quantity $d = |\lambda_1 - \lambda_2| + |\lambda_2 - \lambda_3| + |\lambda_3 - \lambda_1|$, which may be visualized as the perimeter of the triangle formed by the system's three eigenvalues $\boldsymbol{\lambda}$ in the complex plane. At $\boldsymbol{\Psi}_{EP3}$ the three eigenvalues are equal, and so $d = 0$.

The search for the EP_3 point starts with the estimate:

$$\boldsymbol{\Psi}_{EP3}^{(\mathrm{thy})} = (2\pi \times 49.7\ \mathrm{kHz}, 115\ \mu\mathrm{W}, 387\ \mu\mathrm{W}, 285\ \mu\mathrm{W}).$$

We proceed by fixing three of the control parameters to these values, and scanning the fourth (say, Ψ_i). At each value of $\boldsymbol{\Psi}$ in this one-dimensional sweep, $\boldsymbol{\lambda}$ is measured (as described in the Supplementary Information) and converted to $d(\boldsymbol{\Psi})$. The experimental estimate $\boldsymbol{\Psi}_{EP3}^{(\mathrm{est})}$ is then revised with the value of Ψ_i that minimizes d over that sweep. This process is then repeated for different choices of Ψ_i. The estimate resulting from these one-dimensional sweeps is:

$$\boldsymbol{\Psi}_{EP3}^{(\mathrm{est})} = (2\pi \times 49.7\ \mathrm{kHz}, 125\ \mu\mathrm{W}, 435\ \mu\mathrm{W}, 300\ \mu\mathrm{W}).$$

To further refine the estimate of $\boldsymbol{\Psi}_{EP3}$, we then measure $d(\boldsymbol{\Psi})$ on 2D sheets that pass through $\boldsymbol{\Psi}_{EP3}^{(\mathrm{est})}$. For each 2D sheet, two control parameters are scanned while the other two are fixed, resulting in a total of six sheets. The $d(\boldsymbol{\Psi})$ measured on these sheets are shown in Extended Data Fig. 2. For visualization purposes, Extended Data Fig. 3 shows the same sheets, but arranged in 3D to illustrate that $d(\boldsymbol{\Psi})$ is minimized in the neighbourhood of $\boldsymbol{\Psi}_{EP3}^{(\mathrm{est})}$. In Extended Data Figs. 2, 3, the middle row shows the filtered data (see the Supplementary Information for details of the filtering) and the bottom row shows the values of $d(\boldsymbol{\Psi})$ calculated

from H (Supplementary Information) using the best-fit optomechanical parameters determined by fitting the knot, as shown in Fig. 3a,b and described in detail in the Supplementary Information.

Near to $\boldsymbol{\Psi}_{\mathrm{EP3}}$ the quantity $d(\boldsymbol{\Psi})$ is expected to scale as[4] $d(\boldsymbol{\Psi}) \approx |\boldsymbol{\Psi} - \boldsymbol{\Psi}_{\mathrm{EP3}}|^{1/3}$, but in practice the sharp cusp in $d(\boldsymbol{\Psi})$ is broadened by fluctuations in $\boldsymbol{\Psi}$. Nevertheless, clear minima are visible in the measured $d(\boldsymbol{\Psi})$, and their locations are given in the Supplementary Information (Supplementary Table 1). Details of the algorithm used to identify the minima are also in the Supplementary Information. The mean location of these minima is taken as the experimentally identified EP_3:

$$\boldsymbol{\Psi}_{\mathrm{EP3}}^{(\mathrm{exp})} = (\delta_{\mathrm{EP3}}^{(\mathrm{exp})}, P_{1,\mathrm{EP3}}^{(\mathrm{exp})}, P_{2,\mathrm{EP3}}^{(\mathrm{exp})}, P_{3,\mathrm{EP3}}^{(\mathrm{exp})})$$

$$= (2\pi \times 54(7)\,\mathrm{kHz}, 128(8)\ \mu\mathrm{W}, 428(3)\ \mu\mathrm{W}, 304(15)\ \mu\mathrm{W})$$

This compares well with the location of EP_3 that is obtained from the best-fit parameters returned by fitting the measured knot:

$$\boldsymbol{\Psi}_{\mathrm{EP3}}^{(\mathrm{knot})} = (2\pi \times 60.2\,\mathrm{kHz}, 116\,\mu\mathrm{W}, 477\,\mu\mathrm{W}, 329\,\mu\mathrm{W}).$$

Projections of the hypersurface $\mathcal{S}$

Here we describe the two projections that are used in Fig. 3a,b of the main text (as well as Extended Data Fig. 4) to represent data acquired on the hypersurface $\mathcal{S}$, which is the surface of a 4D hyperrectangle.

Standard stereographic projection. Stereographic projection is a standard means for representing a sphere (typically of one, two or three dimensions) in a Euclidean space with the same number of dimensions. In Fig. 3a of the main paper, we represent $\mathcal{S}$ by first projecting it onto the unit three-sphere $\mathcal{S}^3$ and then applying the standard stereographic projection of $\mathcal{S}^3$ onto $\mathbb{R}^3$.

The map is constructed by first adimensionalizing the control parameter as

$$\boldsymbol{\Psi}' := \frac{\boldsymbol{\Psi}}{\boldsymbol{\Psi}_{\mathrm{EP3}}^{(\mathrm{exp})}} - \mathbb{1} := \left(\frac{\delta}{\delta_{\mathrm{EP3}}^{(\mathrm{exp})}} - 1, \frac{P_1}{P_{1,\mathrm{EP3}}^{(\mathrm{exp})}} - 1, \frac{P_2}{P_{2,\mathrm{EP3}}^{(\mathrm{exp})}} - 1, \frac{P_3}{P_{3,\mathrm{EP3}}^{(\mathrm{exp})}} - 1 \right)$$

and then normalizing it as $\boldsymbol{\Psi}'' := \frac{\boldsymbol{\Psi}'}{\|\boldsymbol{\Psi}'\|}$, where $\|\cdot\|$ is the conventional L^2 norm. Note here the implicit use of the fact that $\boldsymbol{\Psi}_{\mathrm{EP3}}^{(\mathrm{exp})}$ lies inside the four-volume bounded by $\mathcal{S}$.

Next, we act on $\boldsymbol{\Psi}''$ with a 4D rotation R (specified below). The new unit vector $R\boldsymbol{\Psi}'' \equiv (x, z, w, y)$ is then stereographically projected onto the 3D cartesian coordinates (X, Y, Z) as $X = \frac{x}{1-w}$, $Y = \frac{y}{1-w}$, $Z = \frac{z}{1-w}$. Thus, the choice of R corresponds to choosing the pole $(x, z, w, y) = (0,0,1,0)$ for the stereographic projection.

The same pole is chosen for all the stereographic projections shown in this work (except for Extended Data Fig. 1, whose generation is described in the Supplementary Material). It is chosen so as to optimize the visualization of the experimentally identified knot, and corresponds to $\boldsymbol{\Psi}'' = (0.1, -0.83, 0.55, 0)$, or equivalently, $\boldsymbol{\Psi} = (2\pi \times 55\,\mathrm{kHz}, 22\,\mu\mathrm{W}, 596\,\mu\mathrm{W}, 304\,\mu\mathrm{W})$.

'Rectilinear stereographic' projection. The projection shown in Fig. 3b of the main text is isomorphic to the projection just described. However, it is intended to provide a more intuitive representation of the dimensionful experimental parameters $\boldsymbol{\Psi}$. Animations that describe this projection are shown in Supplementary Videos 1 and 2.

This projection consists of five steps.

(1) We select one of the eight 3D hyperrectangles that constitute $\mathcal{S}$.

(2) We simply rescale its axes so that it forms a cube (this is the central cube in Fig. 3b).

(3) Each of the six 3D hyperrectangles adjacent to the first one is also rescaled to form a cube, which is then attached to the first cube on their common 2D face. The resulting 'six-way cross' faithfully represents the connections of the central cube to its six neighbours.

(4) To faithfully represent the connections among these six neighbours, a bilinear transformation[43] is applied to each, deforming each cube into a truncated square pyramid. The transformation is chosen so that the 2D faces that are common to any two of these neighbours are made to touch. These seven hexahedrons (the central cube and the six truncated square pyramids surrounding it) can readily be labelled by their original dimensionful axes, as in Fig. 3b. Together they form the bounding box of Fig. 3b.

(5) The final 3D hyperrectangle is mapped to the exterior of the bounding box through a nonlinear mapping, and extends to infinity (as does the standard stereographic projection described above).

As described in the Supplementary Information, there are no EP_2s in the two 3D hyperrectangles that correspond to constant P_1. We choose these to be the interior (cubical) hexahedron and the exterior region. This choice places all of the EP_2s in the six truncated square pyramids, facilitating a clear view of the knot. Supplementary Video 2 gives animated views of the data and fit shown in this projection.

Fitting the EP_2 locations to the optomechanical model

This section describes the fit of the three-mode optomechanical model to the 291 experimentally identified EP_2 points shown in Fig. 3a,b of the main text. These locations are denoted as $\boldsymbol{\Psi}_{\mathrm{EP2}}^{(\mathrm{exp},\ell)}$, with $1 \le \ell \le 291$.

The best-fit parameters $\boldsymbol{\lambda}$ and κ for the model are obtained by minimizing the cost function

$$C(\boldsymbol{g}, \kappa) = \sum_{\ell} |\boldsymbol{\Psi}_{\mathrm{EP2}}^{(\mathrm{exp},\ell)} - \boldsymbol{\Psi}_{\mathrm{EP2}}^{(\mathrm{thy},\ell)}(\boldsymbol{g}, \kappa)|^2$$

where the summands define a distance between the experiment and theory, which is adimensionalized by the EP_3 coordinates $\boldsymbol{\Psi}_{\mathrm{EP3}}^{(\mathrm{exp})} = (\delta_{\mathrm{EP3}}^{(\mathrm{exp})}, P_{1,\mathrm{EP3}}^{(\mathrm{exp})}, P_{2,\mathrm{EP3}}^{(\mathrm{exp})}, P_{3,\mathrm{EP3}}^{(\mathrm{exp})})$.

In particular, for

$$\boldsymbol{\Psi}_{\mathrm{EP2}}^{(\mathrm{exp},\ell)} = (\delta_{\mathrm{EP2}}^{(\mathrm{exp},\ell)}, P_{1,\mathrm{EP2}}^{(\mathrm{exp},\ell)}, P_{2,\mathrm{EP2}}^{(\mathrm{exp},\ell)}, P_{3,\mathrm{EP2}}^{(\mathrm{exp},\ell)})$$

and

$$\boldsymbol{\Psi}_{\mathrm{EP2}}^{(\mathrm{thy},\ell)} = (\delta_{\mathrm{EP2}}^{(\mathrm{thy},\ell)}, P_{1,\mathrm{EP2}}^{(\mathrm{thy},\ell)}, P_{2,\mathrm{EP2}}^{(\mathrm{thy},\ell)}, P_{3,\mathrm{EP2}}^{(\mathrm{thy},\ell)})$$

this dimensionless distance (squared) is

$$|\boldsymbol{\Psi}_{\mathrm{EP2}}^{(\mathrm{exp},\ell)} - \boldsymbol{\Psi}_{\mathrm{EP2}}^{(\mathrm{thy},\ell)}(\boldsymbol{g}, \kappa)|^2$$

$$:= \left(\frac{\delta_{\mathrm{EP2}}^{(\mathrm{exp},\ell)} - \delta_{\mathrm{EP2}}^{(\mathrm{thy},\ell)}}{\delta_{\mathrm{EP3}}^{(\mathrm{exp})}} \right)^2 + \left(\frac{P_{1,\mathrm{EP2}}^{(\mathrm{exp},\ell)} - P_{1,\mathrm{EP2}}^{(\mathrm{thy},\ell)}}{P_{1,\mathrm{EP3}}^{(\mathrm{exp})}} \right)^2 + \left(\frac{P_{2,\mathrm{EP2}}^{(\mathrm{exp},\ell)} - P_{2,\mathrm{EP2}}^{(\mathrm{thy},\ell)}}{P_{2,\mathrm{EP3}}^{(\mathrm{exp})}} \right)^2 + \left(\frac{P_{3,\mathrm{EP2}}^{(\mathrm{exp},\ell)} - P_{3,\mathrm{EP2}}^{(\mathrm{thy},\ell)}}{P_{3,\mathrm{EP3}}^{(\mathrm{exp})}} \right)^2$$

Here, $\boldsymbol{\Psi}_{\mathrm{EP2}}^{(\mathrm{thy},\ell)}(\boldsymbol{g}, \kappa)$ is the EP_2 point found numerically (as a root of the discriminant $D(\boldsymbol{\Psi}, \boldsymbol{g}, \kappa)$, see the Supplementary Information) in a neighbourhood of $\boldsymbol{\Psi}_{\mathrm{EP2}}^{(\mathrm{exp},\ell)}$ and in its 2D data sheet. For example, if $\boldsymbol{\Psi}_{\mathrm{EP2}}^{(\mathrm{exp},\ell)}$ is identified in a data sheet that rasters P_1 and P_2 while holding δ and P_3 fixed, the numerical root is found in the neighbourhood

$$(0.65\ P_{1,\mathrm{EP2}}^{(\mathrm{exp},\ell)}, 1.35\ P_{1,\mathrm{EP2}}^{(\mathrm{exp},\ell)}) \times (0.65\ P_{2,\mathrm{EP2}}^{(\mathrm{exp},\ell)}, 1.35\ P_{2,\mathrm{EP2}}^{(\mathrm{exp},\ell)})$$

at the same fixed values of δ and P_3. $\boldsymbol{\Psi}_{\mathrm{EP2}}^{(\mathrm{thy},\ell)}(\boldsymbol{g}, \kappa)$ is evaluated with $\kappa_{\mathrm{in}}/\kappa = 0.267$, and $\tilde{\boldsymbol{\lambda}}^{(0)}$ held equal to the values determined from the single-tone DBA measurements described in the Supplementary Information.

The minimization of $C(\boldsymbol{g}, \kappa)$ is implemented numerically on a high-performance cluster. The best-fit parameters so obtained are:

$$\boldsymbol{g} = 2\pi \times (0.1979, 0.3442, 0.3092)\text{Hz}$$
$$\kappa = 2\pi \times 173.84\ \text{kHz}$$

These parameters are used to produce the 'best-fit knot' shown as the continuous curve in Fig. 3a,b in the main text. This curve is generated by using the best-fit values of $\boldsymbol{g}$ and κ given just above to calculate $\boldsymbol{\lambda}$ on 16,000 2D sheets in $\mathcal{S}$. On each sheet, the EP_2 points are identified as the roots of the discriminant D (found numerically as described in the Supplementary Information). At each of these EP_2 points, θ is also calculated. Finally, these points are coloured according to θ and are connected by straight line segments.

The values of the parameters $\boldsymbol{g}$ and κ given just above are also used to generate the theory plots in Fig. 2 of the main text, and in Extended Data Figs. 2, 3, 5 and 6 and Supplementary Video 5.

Relation of the present work to studies of non-Hermitian band structure (NHBS)

Topics related to those described in this work have been considered in the context of a NHBS[22,49–59]. However, there are several qualitative differences between NHBS and the non-Hermitian oscillators considered here: in the physical systems being described, the mathematical concepts relevant to the description, and the genericness of the resulting topological structures.

The physical system under consideration in NHBS is a wave propagating in an L-dimensional lattice (in which L is typically 1, 2 or 3) that possesses a combination of non-reciprocity, gain and loss. Propagation in such a lattice can be characterized by bands whose dispersion is given by the complex eigenvalues of a matrix (which plays the role of H in the present paper). A central question in NHBS is how these eigenvalues depend on the quasimomentum $\mathbf{k}$ (whose vector components play the role of the control parameters considered in the present paper). Theoretical[51,56,57] and experimental[22,58] work has shown that varying $\mathbf{k}$ in a closed loop may result in non-trivial eigenvalue braids. Theoretical work has shown that, for some lattices with $L = 3$, two-band systems described by 2×2 matrices may exhibit a trefoil knot of twofold degeneracies within the Brillouin zone[53,54,59]. However, we emphasize that these results are distinct from those presented here.

This is because in NHBS, the number of control parameters is limited to L, and the control space they span (the analogue of $\mathcal{L}_N$ in the present work) is topologically non-trivial by assumption (because the Brillouin zone is an L-torus). By contrast, for non-Hermitian oscillators the control space ($\mathcal{L}_N$) is topologically trivial, and the number of controls (that is, the dimensionality of $\mathcal{L}_N$) is sufficient to span the full space of complex eigenspectra. This results in the direct connection—described in the main text—between non-Hermitian oscillators and general complex polynomials. In particular, the non-trivial structure of the degenerate subspace (which establishes the correspondence between control loops and the non-Abelian group of eigenvalue braids) is a generic feature of $N \times N$ matrices. This is in contrast to NHBS, in which these features are not generic, but only appear on fine tuning.

Last, we note that experiments on NHBS so far[22,58] have been limited to braids realized by two eigenvalues. Thus, they correspond to the $N = 2$ case, for which the subspace of degeneracies has a trivial geometry, and the group formed by the eigenvalue braids is Abelian. By contrast, for the $N = 3$ case explored in the experiments described here, the subspace of degeneracies has a non-trivial geometry, and the eigenvalue braids form a non-Abelian group.

Another approach to studying the propagation of linear excitations in non-Hermitian lattices is provided by gyroscopic metamaterials[60,61]. However, these systems possess purely real eigenvalues (because of the symplectic symmetry of their dynamical matrix), and so do not exhibit the behaviour considered in this work.

Data availability

The experimental data and numerical calculations are available from the corresponding authors upon reasonable request.

Code availability

The code used for data analysis is available from the corresponding author upon reasonable request.

41. Garling, D. J. H. *Galois Theory and its Algebraic Background* 2nd edn 123, 124 (Cambridge Univ. Press, 2021).
42. Milnor, J. *Singular Points of Complex Hypersurfaces* (Princeton Univ. Press, 1968).
43. Henry, P. A. *Measuring the Knot of Non-Hermitian Degeneracies and Non-Abelian Braids*. Thesis, Yale University, New Haven, CT (2022).
44. Buchmann, L. F. & Stamper-Kurn, D. M. Nondegenerate multimode optomechanics. *Phys. Rev. A* **92**, 013851 (2015).
45. Shkarin, A. B. et al. Optically mediated hybridization between two mechanical modes. *Phys. Rev. Lett.* **112**, 013602 (2014).
46. Zhong, Q., Khajavikhan, M., Christodoulides, D. N. & El-Ganainy, R. Winding around non-Hermitian singularities. *Nat. Commun.* **9**, 4808 (2018).
47. Wang, S. et al. Arbitrary order exceptional point induced by photonic spin–orbit interaction in coupled resonators. *Nat. Commun.* **10**, 832 (2019).
48. Xiao, Z., Li, H., Kottos, T. & Alù, A. Enhanced sensing and nondegraded thermal noise performance based on PT-symmetric electronic circuits with a sixth-order exceptional point. *Phys. Rev. Lett.* **123**, 213901 (2019).
49. Makris, K. G., El-Ganainy, R., Christodoulides, D. N. & Musslimani, Z. H. Beam dynamics in PT symmetric optical lattices. *Phys. Rev. Lett.* **100**, 103904 (2008).
50. Szameit, A., Rechtsman, M. C., Bahat-Treidel, O. & Segev, M. PT-symmetry in honeycomb photonic lattices. *Phys. Rev. A* **84**, 021806(R) (2011).
51. Leykam, D., Bliokh, K. Y., Huang, C., Chong, Y. D. & Nori, F. Edge modes, degeneracies, and topological numbers in non-Hermitian systems. *Phys. Rev. Lett.* **118**, 040401 (2017).
52. Chen, W., Lu, H.-Z. & Hou, J. M. Topological semimetals with a double-helix link. *Phys. Rev. B* **96**, 041102(R) (2017).
53. Bi, R., Yan, Z., Lu, L. & Wang, Z. Nodal-knot semimetals. *Phys. Rev. B.* **96**, 201305(R) (2017).
54. Carlström, J. & Bergholtz, E. J. Exceptional links and twisted Fermi ribbons in non-Hermitian systems. *Phys. Rev. A.* **98**, 042114 (2018).
55. Shen, H., Zhen, B. & Fu, L. Topological band theory for non-Hermitian Hamiltonians. *Phys. Rev. Lett.* **120**, 146402 (2018).
56. Wojcik, C. C., Sun, X.-Q., Bzdušek, T. & Fan, S. Homotopy characterization of non-Hermitian Hamiltonians. *Phys. Rev. B.* **101**, 205417 (2020).
57. Hu, H. & Zhao, E. Knots and Non-Hermitian Bloch bands. *Phys. Rev. Lett.* **126**, 010401 (2021).
58. Wang, K., Dutt, A., Wojcik, C. C. & Fan, S. Topological complex-energy braiding of non-Hermitian bands. *Nature* **598**, 59–64 (2021).
59. Zhang, X., Li, G., Liu, Y., Tai, T., Thomale, R. & Lee, C. H. Tidal surface states as fingerprints of non-Hermitian nodal knot metals. *Commun. Phys.* **4**, 47 (2021).
60. Nash, L. M. et al. Topological mechanics of gyroscopic metamaterials. *Proc. Natl Acad. Sci. USA* **112**, 14495–14500 (2015).
61. Mitchell, N. P., Turner, A. M. & Irvine, W. T. M. Real-space origin of topological band gaps, localization, and reentrant phase transitions in gyroscopic metamaterials. *Phys. Rev. E.* **104**, 025007 (2021).

Acknowledgements This work was supported by Air Force Office of Scientific Research award no. FA9550-15-1-0270, Vannevar Bush Faculty Fellowship no. N00014-20-1-2628 and National Science Federation grant no. DMR-1724923. We thank Y. Wang for helpful discussions, and the Yale Center for Research Computing for guidance and use of the research computing infrastructure, specifically M. Guy. J.G.E.H. thanks H. Vanderbilt. J.H. is now supported by Howard Hughes Medical Institute Janelia.

Author contributions N.R. and J.G.E.H. conceived the project. Y.S.S.P., J.H., P.A.H., C.G., L.J. and N.K. designed the experiment. Y.S.S.P., P.A.H. and C.G. took the data. Y.S.S.P., J.H., P.A.H., C.G. and Y.Z. analysed and modelled the data. J.G.E.H. supervised the project. All authors contributed to the writing of the paper.

Competing interests The authors declare no competing interests.

Additional information

Supplementary information The online version contains supplementary material available at https://doi.org/10.1038/s41586-022-04796-w.

Correspondence and requests for materials should be addressed to Yogesh S. S. Patil or Jack G. E. Harris.

Peer review information *Nature* thanks the anonymous reviewers for their contribution to the peer review of this work. Peer reviewer reports are available.

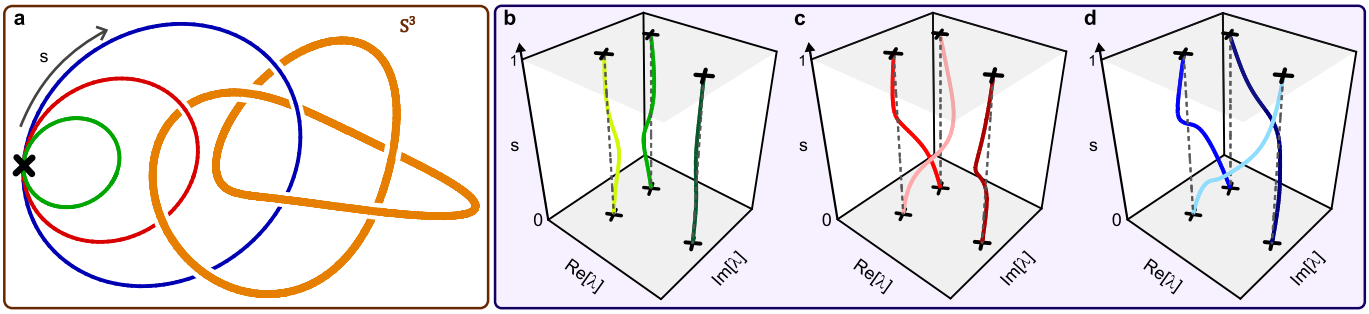

Extended Data Fig. 1 | The trefoil knot of degeneracies and the eigenvalue braids for a three-mode system. a, At a fixed distance from the three-fold degeneracy, the control space for the spectrum is $\mathcal{S}^3$ (shown here in stereographic projection). The degeneracies in this space are all two-fold and form a trefoil knot (orange). Three control loops (green, red, blue), each parameterized by $0 \le s \le 1$ share a common basepoint (black cross). **b**–**d**, Evolution of the eigenvalues as s is varied around each loop in **a**. The black crosses show $\boldsymbol{\lambda}$ at the basepoint. The dashed lines are guides to the eye. This figure is calculated from the characteristic polynomial of a three-mode system (see the Supplementary Information).

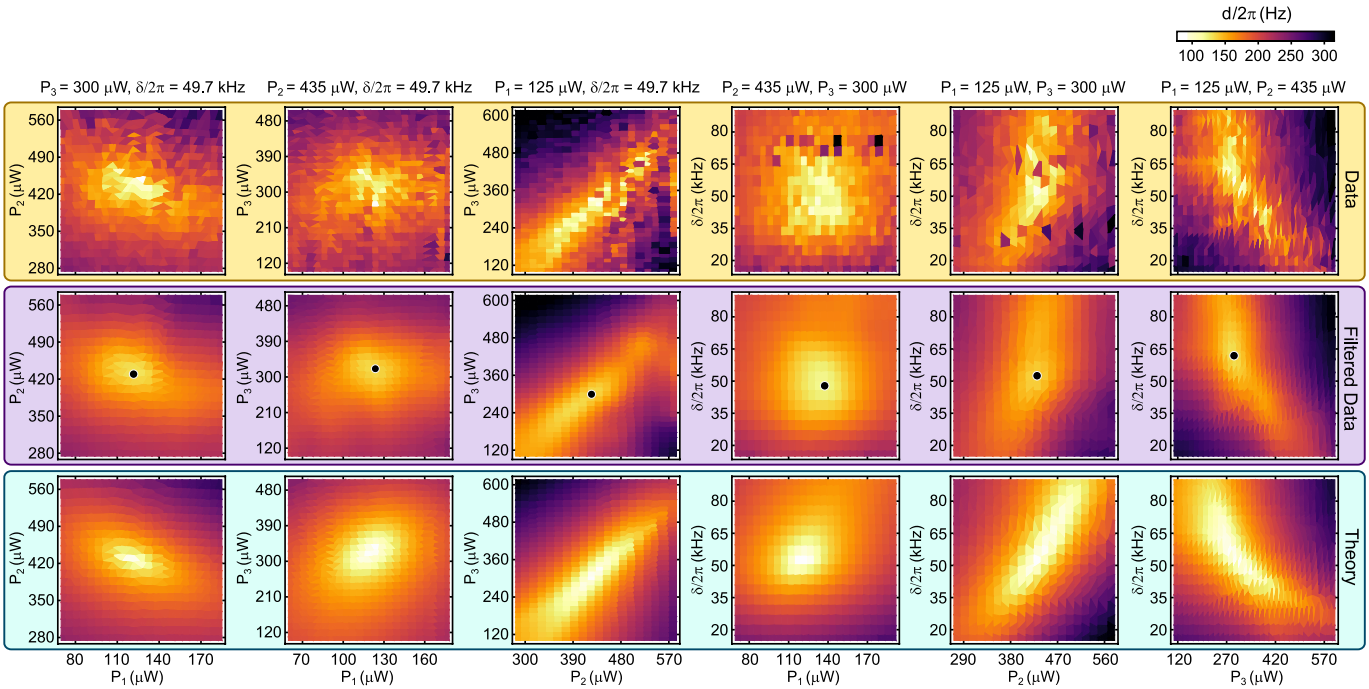

Extended Data Fig. 2 | Locating EP_3. The quantity $d(\boldsymbol{\Psi})$ (which ideally vanishes at $\boldsymbol{\Psi}_{EP3}$), measured on six 2D sheets passing through $\boldsymbol{\Psi}_{EP3}^{(est)}$, the location of the EP_3 that is estimated from scanning individual components of $\boldsymbol{\Psi}$ (Methods). Top row: raw data. Middle row: data after outlier rejection and smoothing described in the Supplementary Information. The black circles show the minima that are located using the algorithm described in the Supplementary Information. Bottom row: the values of d calculated from the optomechanical model.

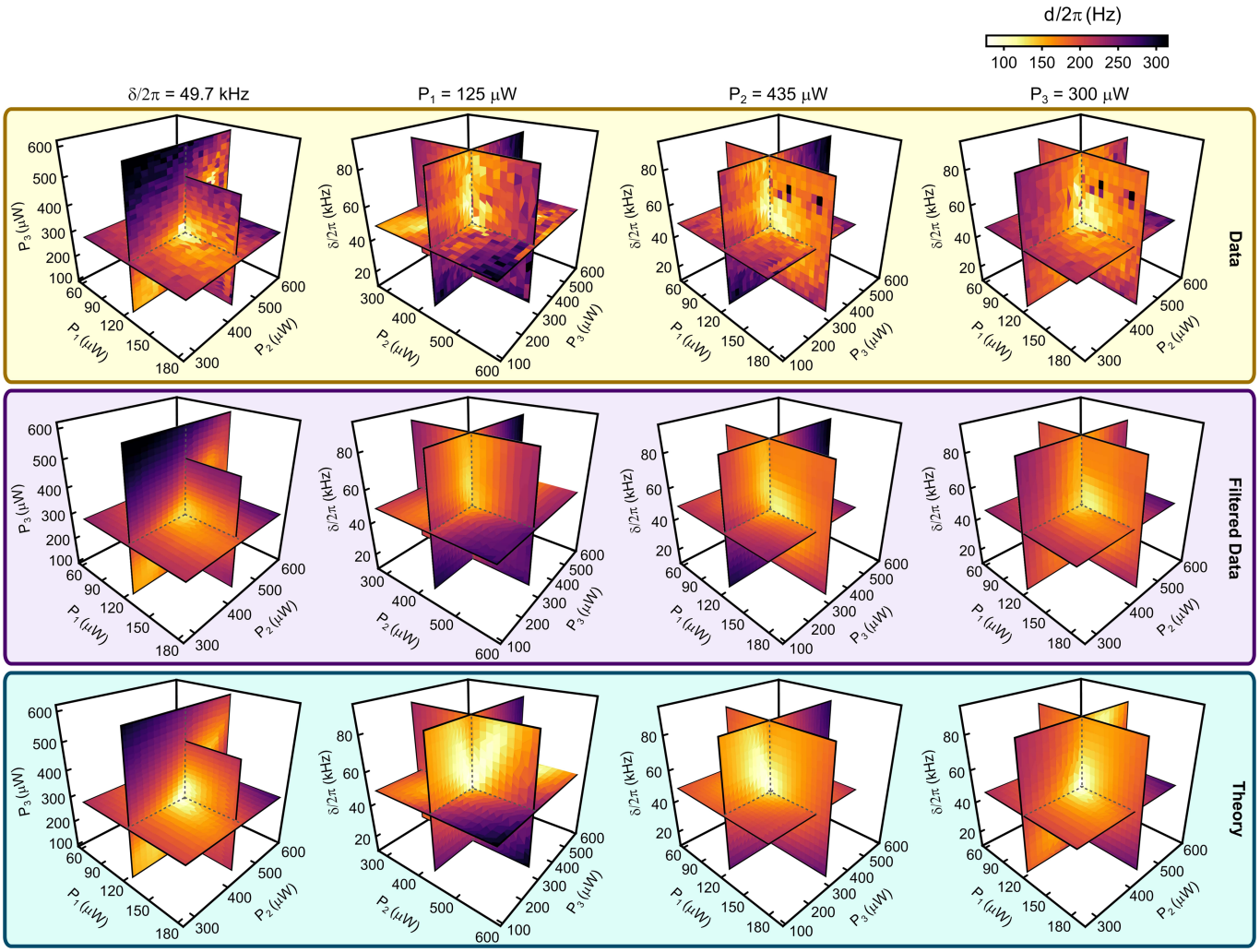

Extended Data Fig. 3 | Locating EP_3 (perspective view). The data of Extended Data Fig. 2 arranged in 3D to illustrate the minimum of $d(\boldsymbol{\Psi})$ in the neighbourhood of the experimentally estimated location of the EP_3.

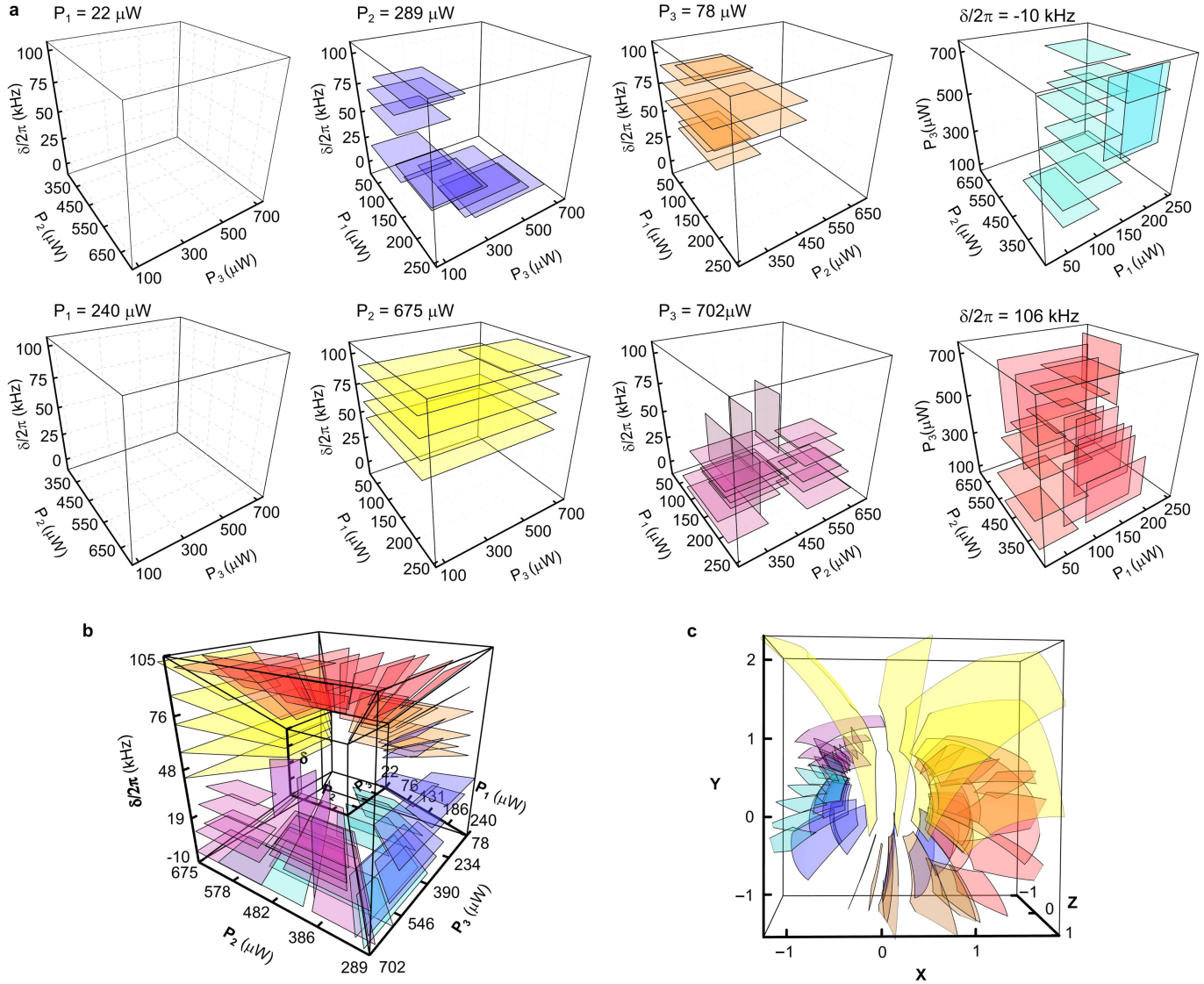

Extended Data Fig. 4 | The locations of the sixty-one 2D sheets within $\mathcal{S}$. The sheets are colour-coded by the 3D face in which they lie. **a**, The sheets are shown within each of the eight 3D faces of $\mathcal{S}$. **b**, The same sheets as in **a**, shown using the 'rectilinear stereographic' projection of Fig. 3b. Note that in this projection, all of the sheets are contained within the plot's bounding box. **c**, The same sheets, shown using the stereographic projection of Fig. 3a. The thin black lines show the boundary of each sheet. Thin grey lines show where a sheet exits the plot's bounding box. The projections are described in Methods. The data from these sheets are shown in Video 5 of the Supplementary Information.

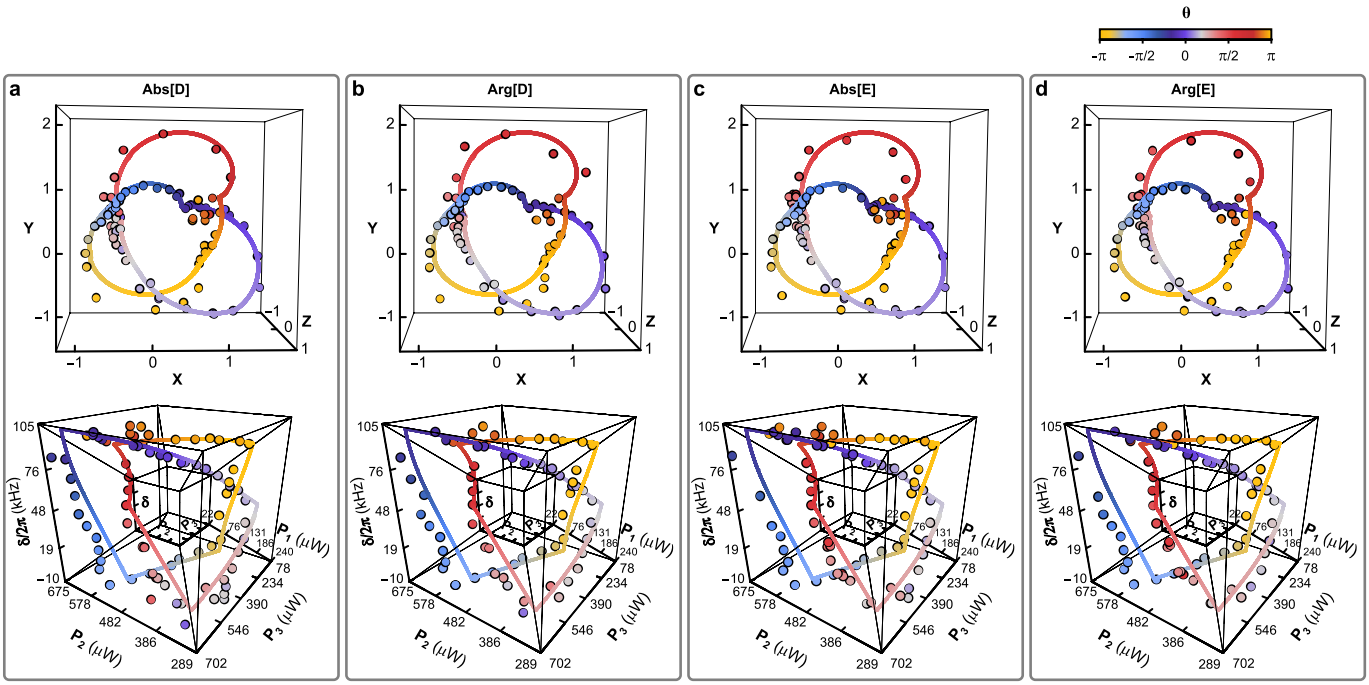

Extended Data Fig. 5 | The knot of EP_2 via four different signatures. The same data as in Fig. 3a, b, but in separate plots for the EP_2 locations determined by each of the four different signatures. **a**, Zeroes of the discriminant D. **b**, Phase vortices of the discriminant D. **c**, Zeroes of the eigenvector indicator E. **d**, Phase vortices of the eigenvector indicator E. The quantities D and E are defined in the main text, and additional discussion of E is in the Supplementary Information. The projections used here are the same as in Fig. 3a, b. The solid curve is the same in all eight panels, and is the best-fit knot shown in Fig. 3a, b.

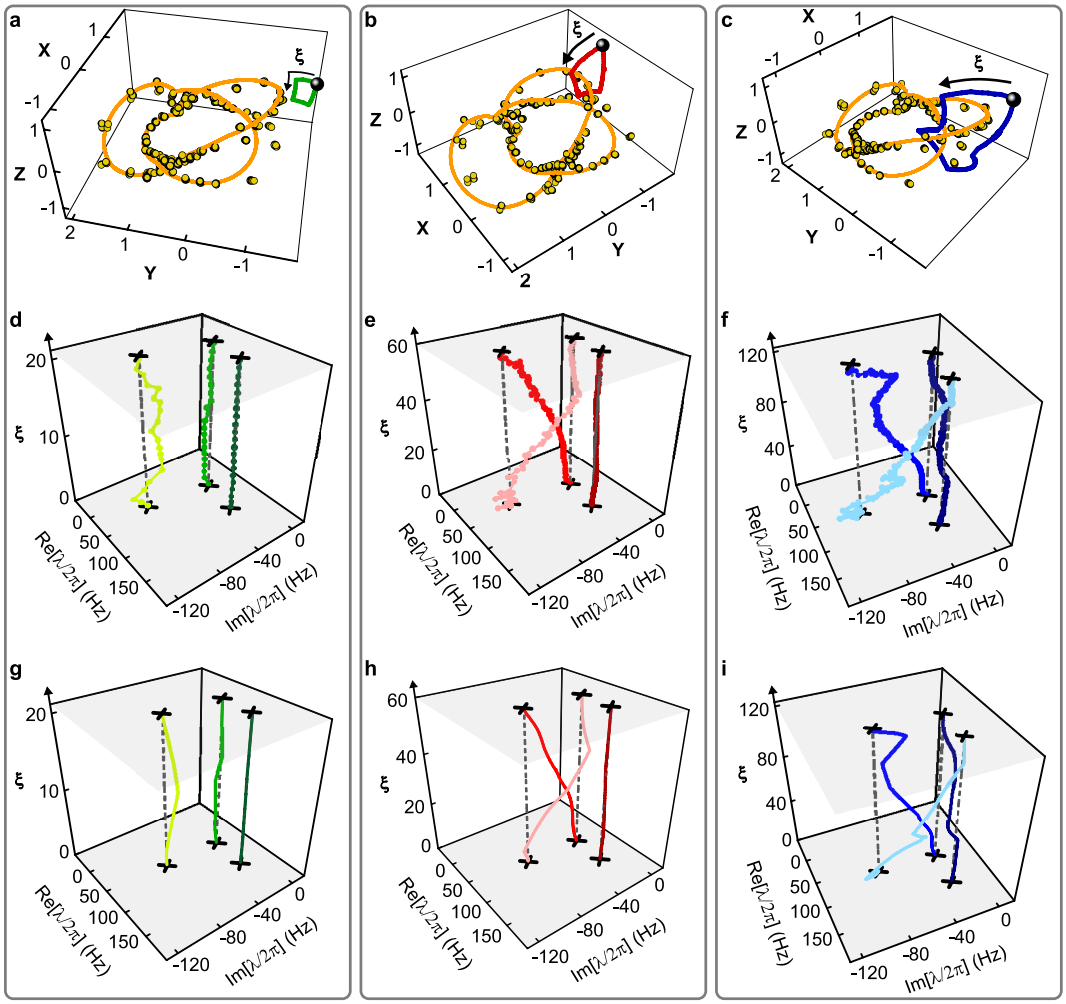

Extended Data Fig. 6 | Comparison of measured and calculated braids. **a**–**f**, The same panels as in Fig. 3c–h. They show the control loops (green, red, and blue in **a**–**c**) in relation to the measured knot (yellow circles) and the best-fit knot (orange curve). **d**–**f**, The resulting eigenvalue braids. **g**–**i**, The eigenvalue spectrum as calculated using the optomechanical parameters determined from fitting the knot of EP_2. The dashed lines are guides to the eye.

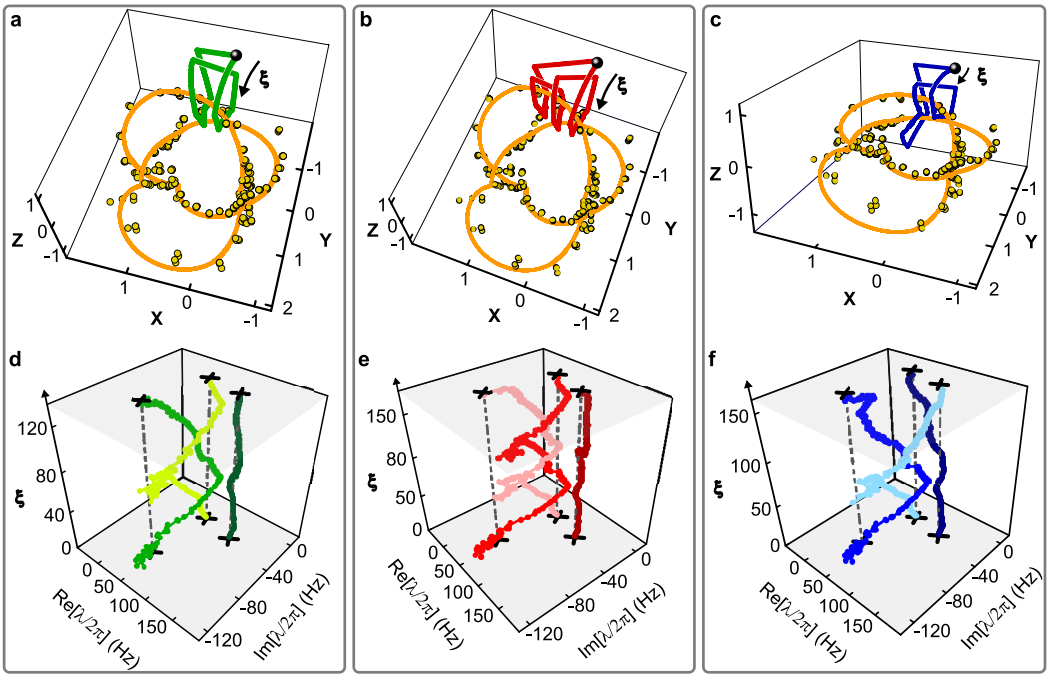

Extended Data Fig. 7 | Additional braids of eigenvalues. a–**c**, Three loops (green, red, blue), each from a different homotopy class. They share a common basepoint (black sphere) and are non-self-intersecting. The measured knot $\mathcal{K}$ (yellow circles) and the best-fit knot (orange curve) are shown for reference. The projection used here is the same as in Fig. 3a. **d**–**f**, The eigenvalue spectrum $\boldsymbol{\lambda}(\boldsymbol{\Psi})$ as $\boldsymbol{\Psi}$ is varied around a loop. The variable ξ indexes the values of $\boldsymbol{\Psi}$ (along each loop) at which $\boldsymbol{\lambda}$ is measured. The black crosses show $\boldsymbol{\lambda}$ at the start and stop of the loop. The dashed lines are guides to the eye. The 1σ confidence intervals for $\boldsymbol{\lambda}$ are comparable to the size of the plotted points. The braids realized are: σ_1^2 (**d**), σ_1^3 (**e**), and $\sigma_2\sigma_1^2$ (**f**).

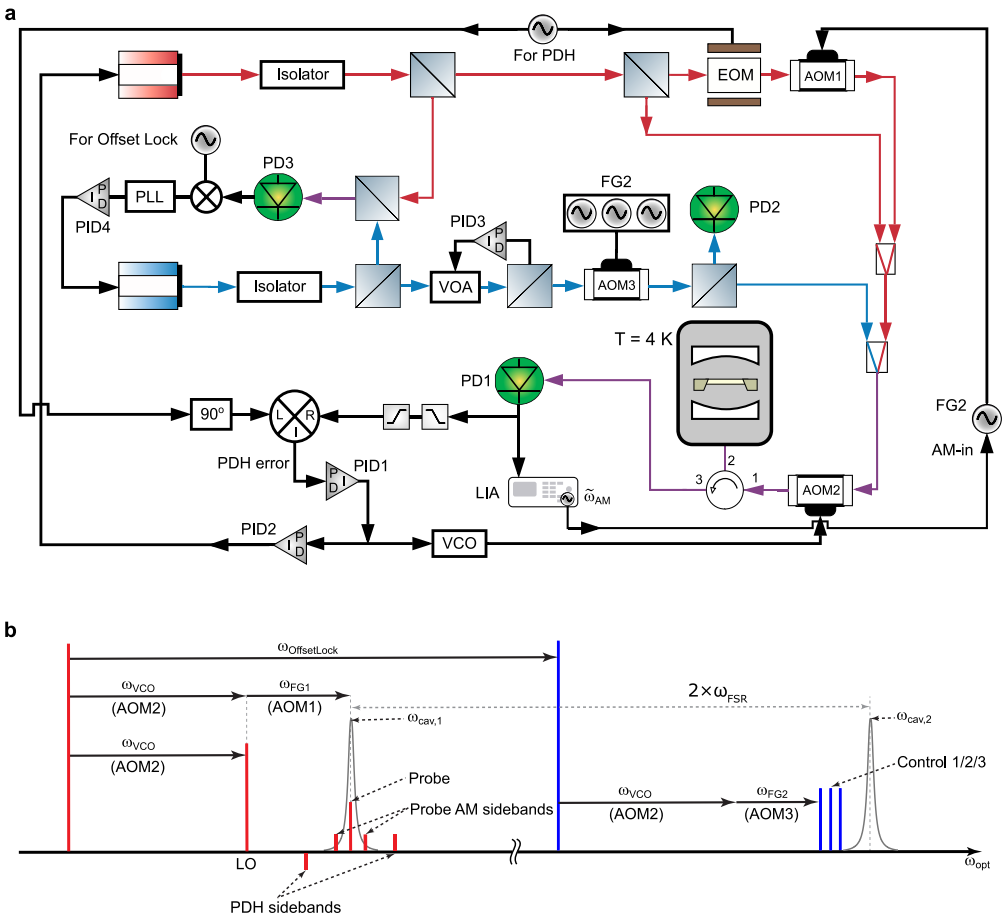

Extended Data Fig. 8 | Details of the experimental setup. a, The optical and electronic layout. Red arrows: beam path from the 'probe' laser. Blue arrows: beam path from the 'control' laser. Purple arrows: overlapped beam path of the two lasers. Black arrows: electronic lines. Grey region: cryostat containing the optical cavity and membrane. The various components are described in the Supplementary Information. **b**, The optical spectrum. Red lines: tones produced from the probe laser. Blue lines: tones produced from the control laser. The tones and their generation are described in Methods and the Supplementary Information. Grey curves: the two cavity modes used in this work.

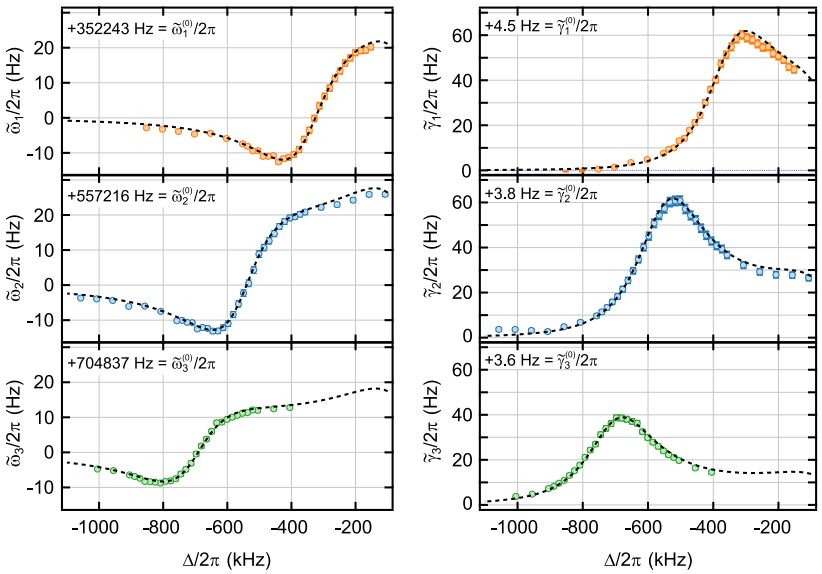

Extended Data Fig. 9 | Characterizing the optomechanical coupling. Here the cavity is driven with a single control tone, whose detuning (from the cavity resonance) is Δ. Each panel shows the measured deviation of the (real or imaginary part of the) mechanical mode's eigenvalue from its bare value (that is, from the relevant component of $\tilde{\boldsymbol{\lambda}}^{(0)}$, whose numerical value is written in the panel). The error bars show the 1σ confidence interval for each data point. A global fit to standard optomechanical theory gives the bare resonance frequencies $\tilde{\boldsymbol{\lambda}}^{(0)}$ and the optomechanical couplings $\boldsymbol{g}$. A detailed description of this procedure is in the Supplementary Information.

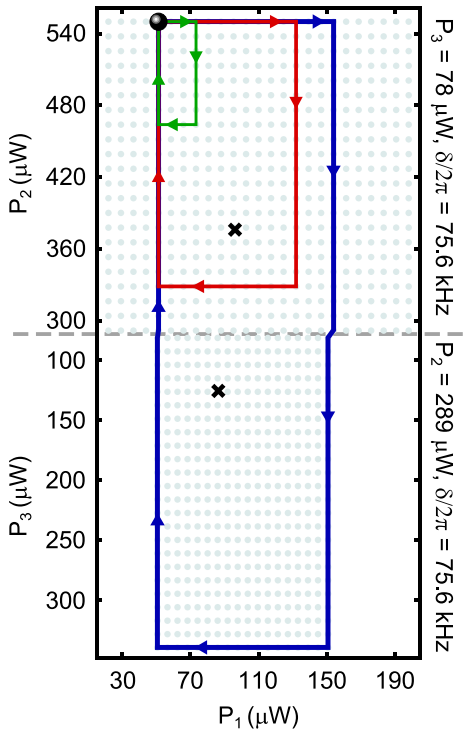

Extended Data Fig. 10 | Control loops from Fig. 3c–e. The three control loops in Fig. 3c–e were assembled from data taken in the two 2D sheets shown here. The two sheets' common border is shown as the dashed grey line. Each small grey disc represents a value of Ψ at which λ was measured (that is, a 'pixel' in the 2D sheet). The black crosses show the location of the EP_2 in these sheets as determined by the minima-finding algorithm described in the Supplementary Information.